Growth and characterization of β-InN films on MgO: the key role of a β-GaN buffer layer in growing cubic InN

H. Navarro-Contreras, M. Pérez Caro, A.G. Rodríguez, E. López-Luna, and M.A. Vidal
Coordinación para la Innovación y la Aplicación de la Ciencia y la Tecnología, Universidad Autónoma de San Luís Potosí, Álvaro Obregón 64, San Luis Potosí, S.L.P. 78000, México.

Recibido el 16 de enero de 2012; aceptado el 9 de febrero de 2012

Cubic InN samples were grown on MgO (001) substrates by gas source molecular beam epitaxy (GSMBE). In general, we find that InN directly deposited onto the MgO substrate results in polycrystalline or columnar films of hexagonal symmetry. We find that adequate conditions to grow the cubic phase of this compound require the growth of an initial cubic GaN buffer interlayer (β-tGaN) on the MgO surface. Subsequently, the growth conditions were optimized to obtain good photoluminescence (PL) emission. The resultant InN growth is mostly cubic, with very small hexagonal inclusions, as confirmed by X-ray diffraction (XRD) and scanning electron microscopy (SEM) studies. Good crystalline quality requires that the samples to be grown under rich Indium metal flux. The cubic β-tInN/GaN/MgO samples exhibit a high signal to noise ratio for PL at low temperatures (20 K). The PL is centered at 0.75 eV and persists at room temperature.

Keywords: A3. Molecular beam epitaxy; B2. semiconducting III-V materials; B1. nitrides; cubic indium nitride.

PACS: 61.05jh; 81.15Hi; 81.05Ea

1. Introduction

For many years, GaN and the Ga-rich $In_xGa_{1-x}N$ and $Al_xGa_{1-x}N$ alloys have been the most studied materials of the entire III-nitride group of compounds and alloys. Actually, there exists a wide range of applications that involve optoelectronic devices, based on those materials, such as green and blue light emission diodes, laser diodes, ultraviolet detectors, high-frequency transistors operating at high power and high temperature, etc [1].

Despite the significant volume of accumulated knowledge and the many published articles about IIIb-nitrides, the binary compound of this group, InN, has remained in comparison relatively unknown. The primary reason for this is that InN is difficult to grow as good quality monocrystalline films.

Previous to the last decade, InN was believed to be a semiconductor with an optical band gap of 1.89 ± 0.01 eV [2]. This value of the band gap was widely accepted and frequently used as the end point value for the extrapolation of the band gap in $In_xGa_{1-x}N$ alloys. [3] However, in recent years, studies performed with good quality wurzite samples, grown by molecular beam epitaxy (MBE) which have substantially reduced free electron concentrations, exhibit band gaps between 0.7 and 0.8 eV [2], values that indicate that InN has the lowest band gap [4,5] of any known IIIb-nitride binary compound or alloy.

Since the mid-infrared band gap of InN was reported, this compound has emerged as a promising material in many applications. The value of the InN infrared band gap suggests the possibility to create devices that operates in optical and mid infrared communications systems. Furthermore, alloying this material with GaN or AlN could tune the band gap across the entire visible range from the mid infrared to deep ultraviolet, a very useful property to produce light emitting devices that emit light at any wavelength of the visible spectrum. An alternative application could be the manufacture of solar cells based on these alloys, which could be optically matched to the solar spectrum.

Other unique properties, in additional to being the compound with the lowest band gap in the binary nitride group, make this material very interesting. For example, theoretical studies have predicted that InN has the smallest effective electron mass in the entire nitride family [6]. Recently O'Leary *et al.*, [7] have shown that InN has a low effective electron mass, although not smaller than of some II-VI semiconductors. This property has the potential to result in high mobility and high saturation velocity for the electrons. Using Monte Carlo simulations, it has been shown that InN has superior electrical transport properties to other compounds in all of the IIIb-nitrides group [8,9], with mobility up to 14000 cm^2/Vs predicted for InN [10], making this material a good candidate for high electron mobility devices. In addition, InN also has the following useful physical properties that make it an important compound to prepare and characterize: i) superior resistance against high-energy particle radiation and (ii) the widest phononic bandgap and narrowest optical phonon band width among all group III-V semiconductors, properties that may be interest to fabricate high efficiency solar cells [4].

It is well known that the members of the IIIb-nitrides group and their ternary alloys crystallize in the thermodynamically stable hexagonal wurzite phase (denoted as α phase). As a result, the majority of the studies with these compounds and ternary alloys have been essentially devoted to the improvement of their crystalline quality as well as all of the other physical properties related to their performance as optoelectronic devices in this phase and InN has not been an exception. However, the cubic phase (denoted as the β phase) of the same group of nitrides (particularly all of the β-

$In_xGa_{1-x}N$ alloys) is expected to possess several advantages over the properties of the hexagonal phase (α-$In_xGa_{1-x}N$), including: 1) higher electron mobility due to higher crystallographic symmetry, and thus lower phonon scattering, 2) higher p-type doping efficiency, and specially, 3) the facility to cleave mirror quality surfaces along the substrate faces for optoelectronic devices and laser applications.

However, its low dissociation temperature ($\sim$550°C) [11] and the difficulty encountered in the preparation of high quality cubic β-InN single crystals have prevented accurate characterization of the basic properties of InN. For these reasons, β-InN has been less studied than β-GaN, β-GaInN, and other similar nitride compounds.

The principal difficulty in the growth of good quality crystals of InN has been the lack of a suitable substrate which minimizes strain during the growth. As a result, the growth of high quality InN crystals still remains as a significant challenge in the fabrication of optoelectronic devices based on crystalline InN.

In this paper, we report the synthesis and characterization of cubic or β-tInN films grown by gas source molecular beam epitaxy (GSMBE) using an In source (99.9999) effusion cell on cubic GaN/MgO (001) substrates in which the recently grown β-GaN buffer layer [12] acts as a template for cubic growth and also minimizes strain in the β-InN film. The high quality β-InN material exhibits continuously flat surfaces, with carrier concentrations between n =10^{19}-10^{20} cm^{-3} due to high In concentration because the InN was grown in Indium rich conditions. The best samples exhibit good quality photoluminescence (PL) at low temperatures (22 to 150 K) centered at 0.70 eV.

2. Experimental details

Details of the GSMBE system may be found elsewhere [13]. The following procedure was performed for all samples grown in this study. Before introduction into the first GSMBE chamber, the MgO substrates were degreased in acetone and isopropyl alcohol, where the preliminary degassing process is carried out. Then the substrates were transferred to the growth chamber. In the more successful InN growths, a β-GaN buffer layer of $\sim$220 nm in thickness is deposited at 600°C on single crystal MgO (001) substrates. These buffer layers are exposed to a nitrogen plasma (with the process parameters described below) to remove any unreacted Ga on the GaN surface. During the InN growth, the substrates were maintained at a fixed temperature, which was chosen in an exploratory fashion in the interval between 320 to 530°C, (growth temperature T_G). The optimum indium effusion cell temperature T_{In} was also explored in the interval 750 to 840°C. The N_2 flow was kept constant at 1.3 sccm and is subjected to a rf power 230 W to form a nitrogen plasma. These growth conditions were chosen in order to obtain good interface and crystalline quality of the samples grown, which was achieved under In-rich conditions and T_{In}= 840 °C. The growth conditions are summarized in Table I.

TABLE I. β-tInN/GaN/MgO, growth conditions.

Sample	Growth Temperature (T_G°C)	Indium Cell Temperature (T_{In}°C)	Growth time (hrs) Thickness (nm)
I3	500	750	1 (80)
I4	500	790	1 (130)
I5	500	840	1 (250)
I8	530	840	1.5
I10	440	840	2
I11	380	840	1.75
I12	320	840	1.5

Photoluminescence (PL) characterization was performed with a half meter monochromator with 300 lines per mm grating, using a He-Ne (638 nm) laser at 20 mW of power, as the excitation source. The samples were placed in a cold finger of a closed-cycle refrigerator to obtain measurements from 10 to 300 K. The detection system consists of an InSb nitrogen cooled detector, and a chopper and lock-in amplifier.

X-ray studies were performed with two different diffractometers. 1) All samples were measured by high-resolution X-ray diffraction (HRXRD), using a Bartels monochromator in the Ge (002) reflection mode, with a Cu anode as the source of X-ray radiation. The X-ray source was operated at 30 kV and 30 mA. Diffraction profiles were obtained from the (004), (224) and (-2-24) reflections to analyze the highly defective and oriented layer grown on the pseudomorphic layer. At each measurement, the sample was tilt adjusted to bring the sample diffraction vector into the diffractometer plane. The angular separation between substrate peak and layer peak reflections was determined by least squares fits to Gaussian profiles in all cases. 2) Additionally, we used the X-ray powder diffraction technique, with a D8 Advance Bruker AXS system, in order to determinate the layers general characteristics such as the existence and relative abundances of cubic and hexagonal phases, among others.

The scanning electronic microscopy (SEM) images were obtained with a Philips FEG-XL30 field emission with an acceleration potential between 10 to 20 kV, depending upon the magnification used in each photography. The EDAX analysis (performed in an EDAX V3.0 Model XL30 system) shows that the InN samples are essentially very closely 50 atomic % In and 50 atomic % N, considering that EDAX is expected to have an intrinsic uncertainty of the order of 3% in percentage determination. Also, some very small quantities of Mg, O and C atoms were found.

3. Results and discussion

The SEM images shown in Fig. 1 illustrate the resultant topography of InN grown at 500 °C on a $\sim$220 nm buffer layer

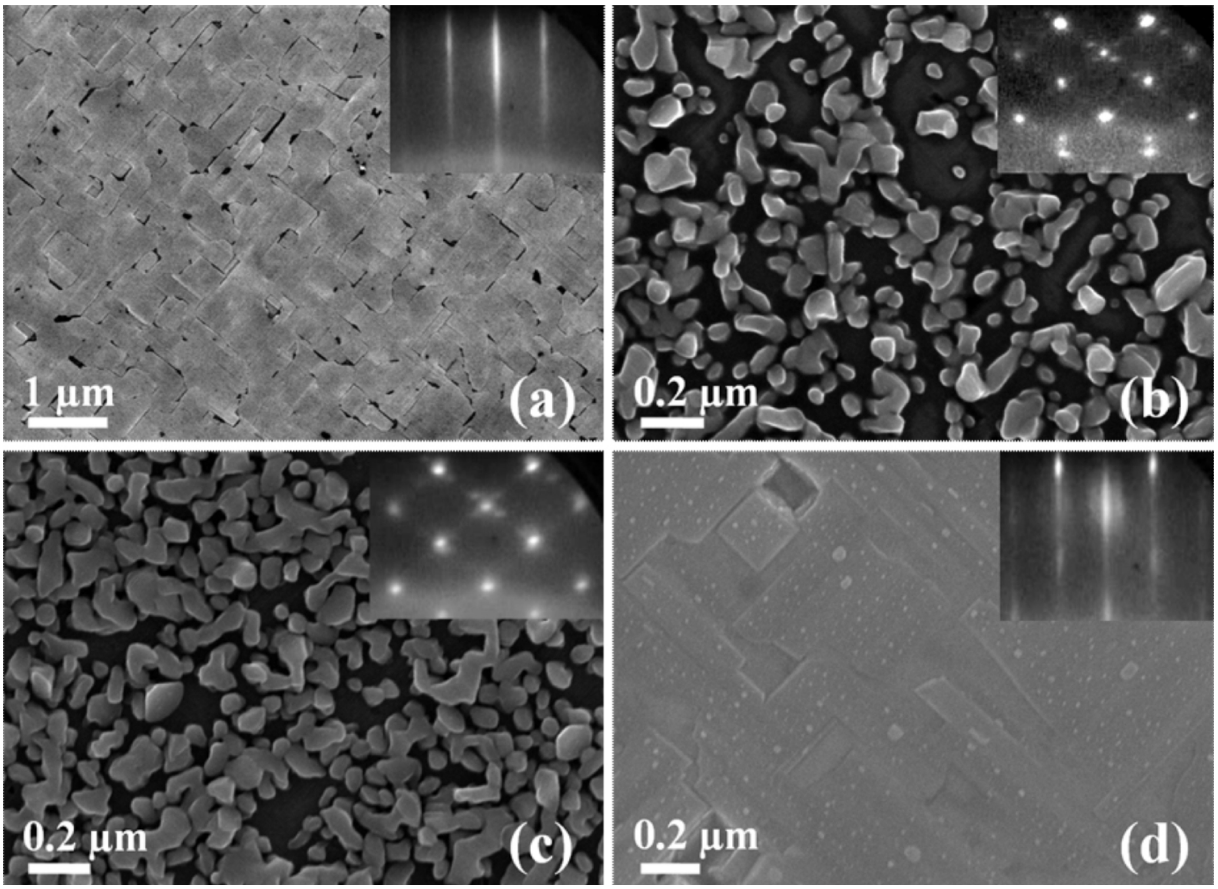

FIGURE 1. SEM images: a) GaN/MgO buffer layer, it is composed by several flat rectangular domains that reflects its cubic symmetry b), c) and d) I3, I4 and I5 β-tInN/GaN/MgO samples. Insets: RHEED patterns.

of β-GaN (see Fig. 1a) supported, in turn, on MgO. The samples were grown at different T_{In} to determine the impact of this parameter on their crystalline quality. Figure 1a shows the β-GaN buffer layer surface composed of several flat rectangular domains that reflect the cubic symmetry of this layer. In addition, the linear streaky RHEED pattern (inset in Fig. 1a) confirms surface diffraction from a cubic structure as well as a good quality, smooth, crystalline surface. These studies suggest that the β-GaN interlayer has the desirable surface quality to promote the growth of β-InN. As seen in Figs. 1b and 1c, InN films grown on β-GaN/MgO structure at T_{In} of 750°C and 790°C have similar characteristics. Both show columnar structures and have similar RHEED patterns (insets in Figs. 1b and 1c) that are spotty, indicating high roughness of the films grown probably caused by the columns. The spots in the patterns are attributable to the relaxed β-InN diffraction structures with in-plane lattice constant of 0.501 nm, estimated from lateral spacing between spots and using the β-GaN RHEED pattern as a reference, yielding a value in close agreement with the accepted value of 0.498 nm [14].

The halos around the diffraction spots may be produced by InN hexagonal phase intrusions in the cubic matrix. The columns seen by SEM are more closely packed as the T_{In} is increased. Hence, it is possible to achieve coalescence of these structures by tuning the In cell temperature during deposition. Figure 1d shows the final topography of a sample grown at T_{In} = 840°C. The surface consists of many flat rectangular-square blocks that reveal the cubic symmetry of the InN film. Identical topography is observed by AFM measurements of the same sample, as reported in Ref. 13. The final blocks are the result of the smoothing or coalescence process performed on the islands previously formed in the initial stages of the β-InN/GaN growth. Also, in this image it is possible to observe very small structures that consists of nano-size droplets of In. From SEM images taken covering large areas (results not shown here), micro-size droplets of In are observed. The presence of this metal in a sample is indicative that the growth was executed under In-metal rich conditions.

At T_{In} = 840°C and at the start of InN growth on the GaN layer, a relaxation process happens, after that, the RHEED patterns were spotty because the relaxation of the large lattice mismatch ($\sim$10%) between β-InN and β-GaN, has taken place. As the growth proceeds, the diffraction spots elongate and sharpen into linear streaks, similar to the RHEED pattern of the completed growth shown as an inset in Fig. 1d. This pattern corroborates the relatively planar surface of β-InN.

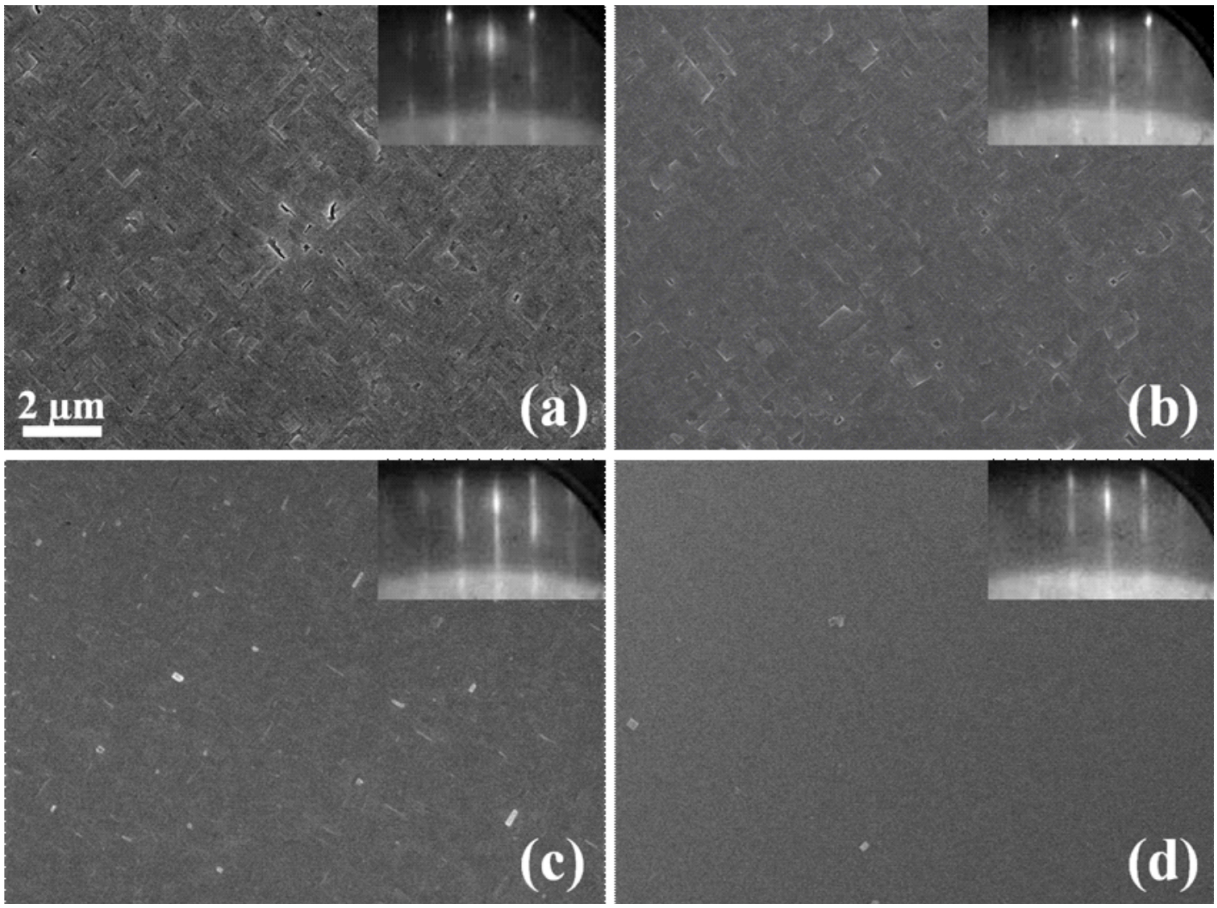

FIGURE 2. SEM images with their corresponding RHEED pattern (insets) for samples a) β-GaN/MgO, the buffer layer prior to the InN growth, b) I3; InN at T_{In} = 750°C, c) I4; InN at T_{In} = 790°C, and d) I5; InN at T_{In} = 840°C.

An in-plane lattice constant of 0.498 nm is calculated from RHEED streaks for this sample. As shown in this photography, β-InN on β-GaN/MgO with good surface quality is successfully grown only under metal rich conditions, such as those present at this larger In cell temperature.

Many β-InN/GaN/MgO samples were grown under In-rich conditions at different substrate growth temperatures T_G to evaluate the quality of the films. Typical SEM images and corresponding RHEED patterns (insets attached to the SEM images) for these samples grown at T_G between 380 to 530°C are shown in Fig. 2. All samples in the Figure were grown under In-rich conditions with T_{In} = 840°C. The SEM pictures in this Figure reveal that all β-InN films have a flat surface. Samples grown at higher substrate temperatures (530 and 500°C, Figs. 2a and 2b, respectively) exhibit more roughness than those grown at lower temperatures (440 and 380°C, Figs. 2c and 2d, respectively). This observation is also supported by the RHEED patterns of the images of each surface. At higher growth temperatures, the RHEED patterns (insets in Fig 2) indicate slight transmission features in the diffraction streaks indicative of some roughness. The SEM image of Fig. 2a shows hollow rectangular pits that may be the cause of those characteristics. However these samples grown at 500 and 530°C have the best structural and optical properties as determined by XRD and photoluminescence studies as discussed below.

To investigate the crystal quality of the InN samples, XRD studies were performed. Figure 3a shows typical XRD curves measured in a θ-2θ configuration of the samples grown in this study. The curves are plotted in a Log scale to be able to recognize very weak signals produced by crystal structures present within the samples. The measurement configuration employed allows the identification of crystal planes that are parallel to the growth plane. Figure 3 provides temperature growth T_G of sample and indium cell temperature T_{In}. The diffractograms correspond to samples with the structure β-InN/GaN/MgO (namely, samples I3, I5, I8, I12). But, to compare these scans, a measurement of a hexagonal sample, with structure α-InN/MgO (sample I9, with following growth conditions, T_G= 500°C, T_{In}= 840°C) is included at the top. For clarity, all curves are plotted with the same intensity scale. To elucidate some diffraction characteristics, the XRD signal of the MgO substrate is also plotted at the bottom part of the Figure. Diffraction maxima at 2θ=42.92, 39.85, and 36.04 degrees, indicated as dashed lines in Fig. 3, are assigned to the (002) diffraction corresponding to the MgO substrate, β-GaN buffer layer and β-InN film, respectively. As shown in this figure, the diffraction peaks of β-GaN and

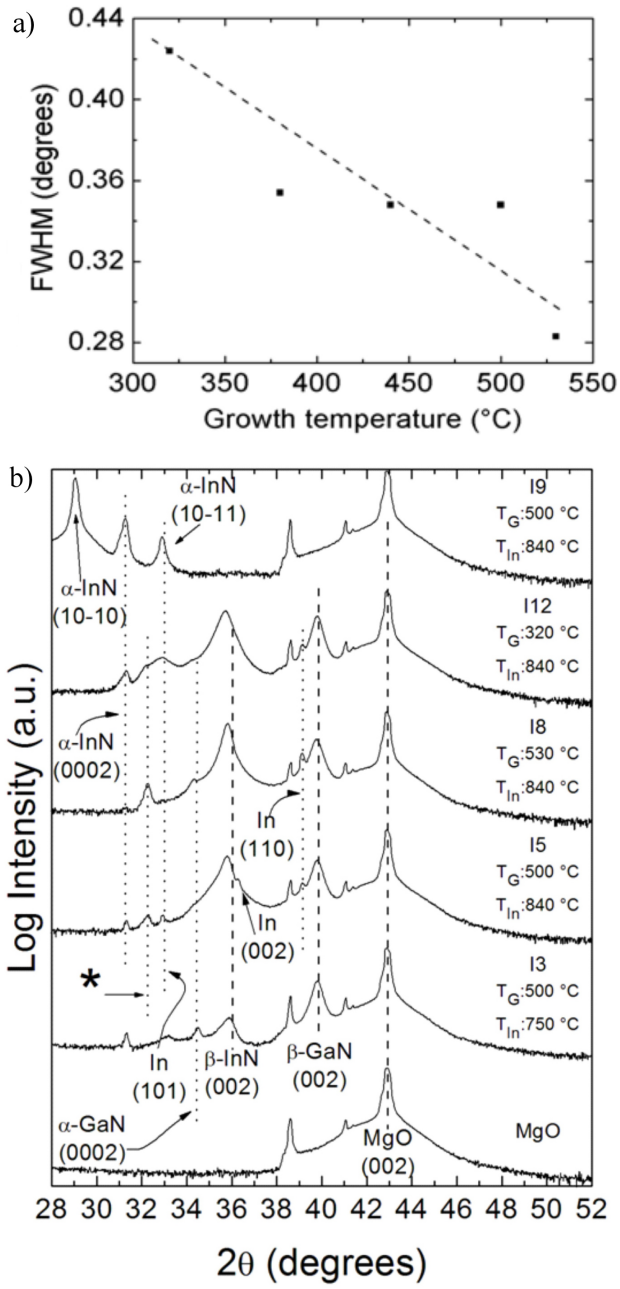

FIGURE 3. X-ray powder diffraction curves, in a θ-2θ configuration, for β-tInN/GaN/MgO, from 28° to 52°, for some of the samples studied in this work. Dotted lines are included for visual aid to identify peaks nature.

β-InN of each sample are slightly shifted from the bulk positions (a_{MgO} = 4.212 Å, 2Θg 42.94, a_β-GaN = 4.52 Å, 2Θg 39.84 and a_β-InN = 4.98 Å, 2Θg 36.02 respectively) which indicate that in these materials there are some residual strains. All samples exhibit XRD peaks at ∼38.6° and 41°, which are attributed to the MgO substrate. For columnar sample I3, it is seen that the XRD indicates that most of the InN columns have cubic symmetry. However, diffraction peaks assigned to α-InN are observed from the hexagonal planes (0002) and (101) for this sample. The flat InN epilayer of

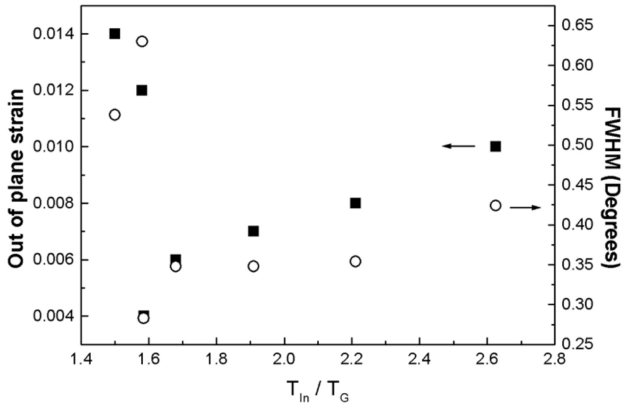

FIGURE 4. Behavior of the (002) diffraction FWHM, (solid squares) and out of plane residual strain (open circles) with the ratio T_{In}/T_G.

sample I5, grown at the similar conditions as I3 but at T_{In}=840°C, shows an increment of the cubic structure (002) related peak, and how all the hexagonal features have almost disappeared. A pair of peaks in the XRD pattern of sample I5 at 2θ ∼39.15° and 36.3° are attributed to the (110) and (002) reflections, respectively, from the In tetragonal structure. The In metal signal (from the tetragonal structure) is present because the growth was executed under In-rich environment as confirmed by metal droplets observed by SEM, as has been already mentioned before. Here, it should be noted that an additional peak of Indium from planes (101) is located at 32.93°.

The β-InN film of sample I8, grown at the highest substrate temperature (T_G = 530°C) and optimal In cell temperature T_{In} of 840°C, has a (002) peak with the narrowest full width at half maximum (FWHM), see Fig. 3b and Table II. Clearly, the structural quality of β-InN improves when the temperature of the In cell is increased and the growth temperature is lowered from the InN decomposition temperature of ∼ 550°C [11]. However, if T_G is further decreased the (002) peak widens and the (0002) reflection of hexagonal α-InN increases. Figure 4 shows the behavior of the (002) diffraction peak at FWHM and out of plane residual strain with the ratio T_{In}/T_G. The Figure suggests that the optimal conditions for higher structural quality, *i.e.* lower FWHM and residual strain, are those used to prepare sample I8 (T_G=530°C, T_{In}=840°C). Sample I5 (T_G=500°C, T_{In}=790°C), the sample next in quality, when judged by the same X-ray FWHM criterion, has relatively some slightly lower crystalline quality; however, if judged by the PL intensity, sample I5 exhibited the best PL emission. In Table II and Fig. 4 it may corroborated that these two samples exhibit the smallest values of residual strain present. Considering these results for the lowest FWHM in XRD, smaller residual strain and efficiency of PL, it may be concluded that the optimal conditions to grow cubic InN in the MBE system lies somewhere between T_G=500 to 530°C and T_{In}= 790 to 840°C

TABLE II. β-tInN/GaN/MgO, HRXRD results and lattice characteristics.

Sample	T_{In} / T_G	$a_\perp$ (nm)	$a_?$ (nm)	a_{bulk} (nm)	FHWM (degree)	$\varepsilon_\perp$ g(X10^{-3})	$\varepsilon_?$ g(X10^{-3})
I3	1.50	0.5027	0.5039	0.5039	0.538	14	9
I4	1.58	0.5017	0.5028	0.5028	0.630	12	7
I5	1.68	0.4970	0.4989	0.4989	0.348	6	-2
I8	1.584	0.4968	0.4982	0.4982	0.283	4	-2
I10	1.91	0.4975	0.4993	0.4993	0.348	7	-1
I11	2.21	0.4984	0.5001	0.5001	0.354	8	0.8
I12	2.63	0.5005	0.5016	0.5016	0.424	10	5

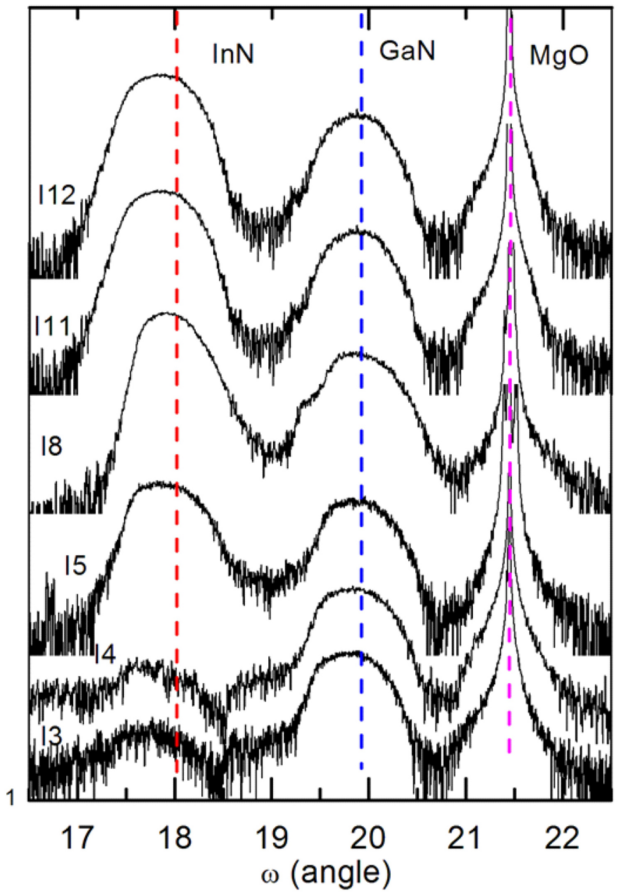

FIGURE 5. High resolution X-ray diffraction spectra of β-tInN/GaN/MgO. The deviation among the dotted line at the lower angles side and the β-tInN broad maxima, provides a visual indication of the residual strain in the sample.

Following the procedure given in Ref. 15 the dominance of the cubic phase of the GaN interlayer was estimated to be $>$ 99 %, from the ratio of the integrated intensities of high resolution X-ray diffraction cubic [002] and hexagonal [1011] rocking curves. We find that the β-InN films grown in our system have cubic content from 92 % to 98 % for those samples that exhibit good crystalline properties and have continuous flat surface, namely samples ranging from I5 to I12.

Comparison of the XRD patterns of structures InN/MgO and InN/GaN/MgO is an interesting exercise. Sample I9, with no β-GaN buffer layer, shows the unexpected result that in spite of growing InN directly on a cubic substrate, it produces no XRD signal from the cubic phase. This highly oriented polycrystalline sample exhibits peaks only from the hexagonal phase. It is possible to distinguish diffraction by the hexagonal planes (100), (0002) and (101). The (100) peak is that of maximum relative strength. Thus, preferential growth of α-InN occurs with planes (100) parallel to the (001) MgO planes. Although this growth was performed at T_{In} = 840°C, there is no evidence of diffraction from In droplets, indicating that *most of the In is being incorporated during the hexagonal growth*, contrasting with all other samples grown at similar temperature with the GaN buffer layer, conditions that resulted in good quality and predominant cubic XRD features. This result as well as others observed for direct growth of InN on MgO established the condition that in order to grow good quality β-InN films, the necessary hetero structure consists of InN/GaN/MgO, *i.e.* it requires the presence of a β-GaN buffer layer.

In order to determinate the lattice parameter and residual strain of the β-InN layers, we used the HRXRD. The lattice parameters were obtained using two procedures. First, from the diffraction position for the (002) planes in β-InN (see Fig. 5): the in-growth lattice parameter ($a\perp$) was measured, while the in-plane lattice parameter ($a||$) was calculated using second order elastic constants, C_{11}=187 GPa and C_{12}=125 GPa, the elastic constants for β-InN (16). Secondly, using the asymmetric diffractions from the (224) and (-2-24) planes (not shown), the in-plane and in-growth lattice parameters were experimentally calculated following the procedure described by Ladrón de Guevara, *et. al.*, [17].

The results are presented in Table II that summarizes the observed variations in the in-growth ($a\perp$) and in-surface ($a||$) lattice parameters for the samples studied. Table and II and Figs. 4 and 5 show how the strain and the bulk lattice constant are minimal at T_G = 530°C and T_{In} 840°C (sample I8). Diminishing of either T_G or T_{In} from these values, tends to increase the strain. The origin of these lattice parameter variations and of the residual strain may stem from the fact that the β-InN films are formed by countless flat rectangular do-

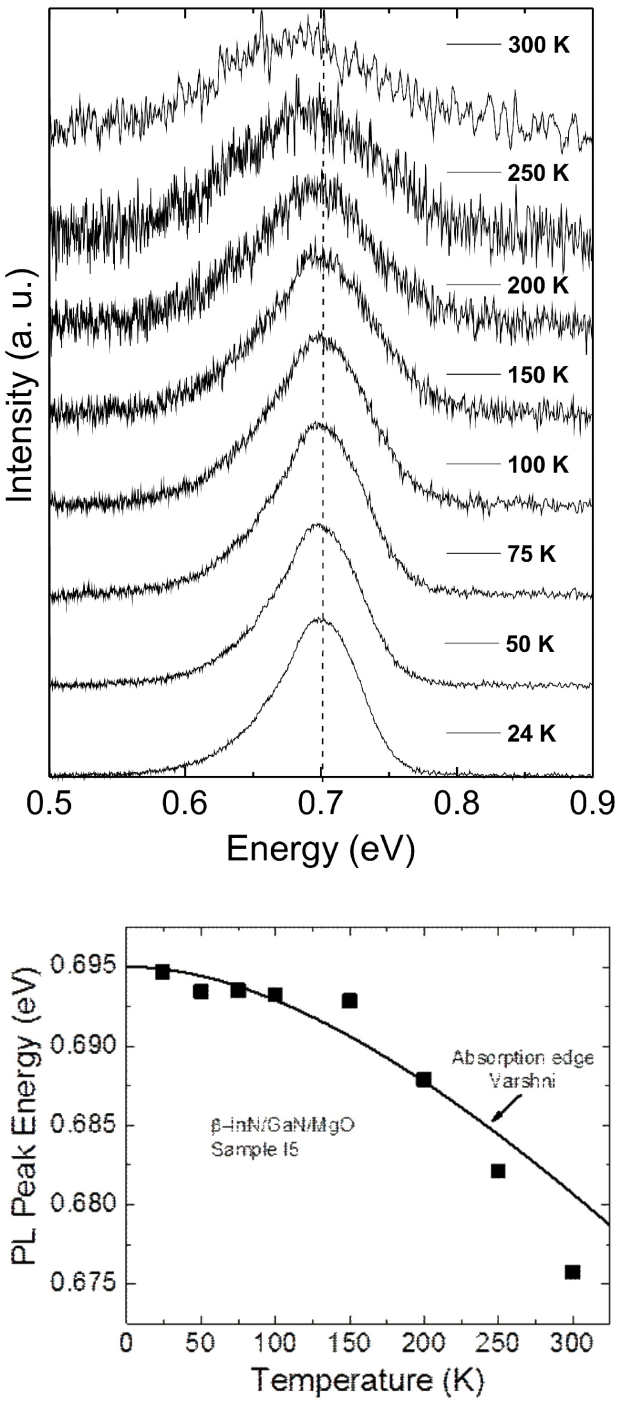

FIGURE 6. PL of β-InN/GaN/MgO, Sample I5, from 10 K to room temperature. b) Plot of PL peak positions. Solid line: the Varshni fit at 1.088 eV, of the absorption edge of this sample downshifted to coincide at zero K with the extrapolation of the PL peak at the same temperature.

mains that press against each other during the growth process, producing stress at their borders.

Optical studies based on PL were conducted to evaluate the emission properties of the samples grown. Figure 6 shows the temperature evolution of typical PL spectra of the β-InN/GaN/MgO I5 cubic sample with temperature. The spectra exhibit luminescence centered around 0.7 eV at 24 K and at 0.67 eV at 300 K. The PL in the sample follows a Varshni-like temperature response, indicative of transitions from either localized states near or from the bottom of the conduction band to the valence band. This identification is reinforced by the observation that actual total energy change in the PL peak positions from low temperature (LT) to room temperature (RT) $\sim$20 meV, is quite comparable in magnitude with the $\sim$15 meV similar temperature shift reported for the absorption edge for this sample, located at 1.088 eV [18]. The 5 meV difference between these two energy shifts has probably no special meaning, because of the PL peak position has a large uncertainty, especially above 200 K. In addition, we are comparing here the energy shifts of the renormalized conduction bands at essentially different **k** vector positions: those close to zero for the PL, which is below the onset of the conduction band, and at the Fermi $\mathbf{k}_f$, vector which corresponds to the Fermi energy position that invades the conduction band at more than 300 meV above the $\sim$0.6 eV conduction band minimum, for the absorption edge, as expected for these degenerated samples.

The PL of this I5 sample (our best result), with carrier concentration n= 5.7$\times$10^{19} cm^{-3}, exhibits higher signal to noise characteristics than those found in the literature for MBE grown β-InN [18-20], and hence far larger intensity, at least at LT. The PL line shape is asymmetric exhibiting a more extended low energy side. In Ref. 21, similar emission centered at 0.69 eV at 10 K, has been published for a sample with carrier concentration n= 1.7$\times$10^{19} cm^{-3}, that exhibits a similar asymmetric profile, after fitting with a lineshape derived from the renormalized band gap $E_g(n)$, from the work of V.Y. Davidov *et. al.*, [22]. It is interesting that in our case, we find from the onset at the low energy side of the PL in Fig. 5 at 24 K, an almost identical value as that of Ref. 23, of $E_g(n)$= 0.56 eV, although our sample may contain at least three times more carriers in the conduction band.

In contrast, the PL of InN grown directly on a bare MgO substrate (with no GaN buffer layer), also exhibited PL signals (not shown). The PL of these hexagonal samples is centered at 0.75 eV at low temperatures. For all those samples, the PL observed is always noisier compared with that of the β-InN/Gan/MgO reported in this work.

One of the goals of growing and studying the β-tInN is to achieve material with emission properties in their infrared band-gap or absorption edges. There are few other reports of room temperature PL of β-tInN, mostly from sputter deposition material, most of them exhibit emission at substantially higher frequencies, at energies between 1.3 and 1.9 eV, which may be due not to cubic InN but to In_2O_3 [24,25]. In our study, most of the samples exhibit PL emission up to room temperature, satisfying our objective, with β-tInN/GaN/MgO displaying better emission at the desired wavelengths centered on 0.7 eV (0.75 eV for the hexagonally dominated InN/MgO).

4. Conclusions

In summary, we have optimized the conditions to grow by molecular beam epitaxy good crystalline quality cubic InN, or β-InN/GaN/MgO. The prior growth of a GaN buffer layer was found to be essential to achieve good quality β-tInN films. Similarly, it was necessary to grow the samples under In-rich conditions. The β-tInN/GaN/MgO samples grown under the optimized set of conditions exhibit good signal to noise ratio photoluminescence at low temperatures (24 K) which persists at room temperature, centered at 0.7 eV, for the cubic material.

5. Acknowledgements

The authors acknowledge the financial support from Consejo Nacional de Ciencia y Tecnología (CONACyT) through grants 152155, México; from FAI-UASLP, and FRC-UASLP, as well as the access to the facilities of the Laboratorio Nacional de Nanomateriales-IPICYT, during the course of this research.

1. S. Nakamura, S. Pearton and G. Fasol, *The Blue Laser Diode: The Complete Story* (Berlin: Springer 2000).
2. T.L. Tansley and C.P. Foley, *J. Appl. Phys.* **59** (1986) 3241.
3. C. Wetzel, T. Takeuchi, S. Yamaguchi, H. Katoh, H. Amano, and I. Akasaki, *Appl. Phys. Lett.* **73** (1998) 1994.
4. J. Wu, W. Walukiewicz, K.M. Yu, J.W. Ager III, E.E. Haller, Hai Lu, W.J. Schaff, Yoshiki Saito, Yasushi Nanishi, *Appl. Phys. Lett.* **80** (2002) 3967.
5. W. Walukiewicz, J.W. Ager III, K.M. Yu, Z. Liliental-Weber, J. Wu, S.X. Li, R.E. Jones and J.D. Denlinger, *J. Phys. D: Appl. Phys.* **39** (2006) R83.
6. P. Rinke, M. Winkelnkemper, A. Qteish, D. Bimberg, J. Neugebauer, and M. Scheffler, *Phys. Rev. B* **77** (2008) 075202.
7. S.K. O'Leary, B.E. Foutz, M.S. Shur, L.F. Eastmand, *Solid State Commun.* **150** (2010) 2182.
8. S.K. O'leary, B.E. Foutz, M.S. Shur, U.V. Bhapkar, and L.F. Eastman, *J. Appl. Phys.* **83** (1998) 826.
9. S.K. O'Leary, B.E. Foutz, M.S. Shur, and L.F. Eastman, *Appl. Phys. Lett.* **88** (2006) 152113.
10. V. M. Polyatov and F. Schwierz, *Appl. Phys. Lett.* **88** (2006) 032101.
11. Y. Nanishi, Y.Saito, T. Yamaguchi, *Jpn. J. Appl. Phys.* **42** (2003) 2549.
12. M. Pérez Caro, Alfredo Campos Mejía, A.G. Rodríguez, H. Navarro-Contreras, and M.A. Vidal, *J. Crystal Growth.* **311** (2009) 1302.
13. Doctoral Thesis, M. Pérez Caro (in Spanish). (Universidad Autónoma de San Luís Potosí, México August 2009), unpublished.
14. I. Vurgaftman and J.R. Meyer, *J. Appl. Phys.* **94** (2003) 3675.
15. H. Tsuchiya, K. Sunaba, S. Yonemura, T. Suemasu and F. Hasegawa, *Jpn. J. Appl. Phys.* **36** (1997) L1-L3.
16. M.A. Moram and M.E. Vickers, *Rep. Prog. Phys.* **72** (2009) 036502.
17. H. Pérez Ladrón de Guevara, A. Gaona-Couto, M.A. Vidal, J. Luyo Alvarado, M. Meléndez Lira and M. López-López, *J. Phys. D: Appl. Phys.* **35** (2002 1408).
18. M. Pérez-Caro, A.G. Rodríguez, M.A. Vidal, and H. Navarro-Contreras, *J. Appl. Phys.* **108** (2010) 013507.
19. P. Schley, R. Goldhahn, C. Napierala, G. Gobsch, J. Schörmann, D.J. As, K. Lischka, M. Feneberg, and K. Thonke, *Semicond. Sci. Technol.* **23**, (2008) 055001.
20. J. Schörmann, D.J. As, K. Lischka, P. Schley, R. Goldhahn, S.F. Li, W. Löffler, M. Hetterich, and H. Kalt, *Appl. Phys. Lett.* **89** (2006) 261903.
21. M. Pérez-Caro, A.G. Rodríguez, M.A. Vidal, and H. Navarro-Contreras, *J. Appl. Phys.* **108** (2010) 013507.
22. V.Y. Davydov *et al.*, *Phys. Status Solidi B* **234** (2002) 787.
23. P. Schley *et al.*, *Phys. Status Solidi b* **246** (2007) 1177.
24. T. Sasaoka, M. Mori, T. Miyazaki, and S. Adachi. *J. Appl. Phys.* **108** (2010) 063538.
25. Q. X. Gao, T. Tanaka, M. Nishio, H. Ogawa, D. Pu, and W.Z. Shen. *Appl. Phys. Lett.* **86** (2005) 231913.